Geochemical Perspectives Letters

Earth's first glaciation at 2.9 Ga revealed by triple oxygen isotopes

A. Hofmann, I.N. Bindeman

Supplementary Information

The Supplementary Information includes:

- Methods
- Supplementary Tables S-1 to S-3
- Supplementary Figures S-1 to S-5
- Supplementary Information References

Methods

Major element contents of powdered samples were determined using a Panalytical MagiX PRO X-ray fluorescence spectrometer housed at the University of Johannesburg's SPECTRUM analytical facility on fusion discs. USGS and GSJ standard reference samples were used for calibration (Table S-2). Detection limits are conservatively estimated at 0.05 wt. %. CIA values were determined using the procedure of Nesbitt and Young (1982), with CaO corrected for apatite content only as samples lack carbonate.

Raman analyses were carried out on thin sections using a WITec alpha300R confocal laser Raman microscope configured with a frequency-doubled Nd-YAG laser (wavelength 532 nm) at the Department of Geology, University of Johannesburg. Raman spectra and maps were collected using a 20× Nikon objective. A laser power of 4 mW was used to prevent thermal degradation of magnetite. Beam centering and Raman spectra calibration were performed before spectral acquisition using a Si standard (111).

Measurement of ^{17}O values relied on 1–2 mg of material after drying them under vacuum at 200 °C overnight in a vacuum oven. The oxygen from the samples was extracted by a 35 W MIR-10 Laser, using BrF_5-laser fluorination line coupled with a MAT253 mass spectrometer at University of Oregon, USA (Bindeman *et al*., 2022). The extracted O_2 was purified by first cryogenic purification, then via boiling Hg, and then frozen on the first 5A molecular sieve held at LN2 temperatures. We then used a home-built GC-based purification system and passed O_2 in the flow of He (10 mL/min) through 5A 8-ft-long column. This separates O_2 from NF_x components causing molecular interferences on mass 33. Gas was then frozen on the second molecular sieve loop by LN2 and further purified by an ethanol-dry ice slush at −114 °C to further remove any molecules interfering with mass 33 (e.g., NF). The gas was then frozen on a zeolite finger in front of the mass spectrometer and expanded into bellows; it was analysed in dual inlet mode for 3 cycles of eight repetitions each against gas from the University of Washington, calibrated relative to VSMOW. A set of international (SCO, UWG-2) and in-house standards comprising of chert (KFKS, Miller *et al*., 2020) were used to calibrate the raw values with respect to the VSMOW scale. Typically, long-term mantle (SCO) value we obtain is $\Delta'^{17}O_{0.528} = -0.037$ ‰ and we adjusted measured values downward by 10−20 ppm $\Delta'^{17}O$ to match the theoretical values of standards, and this amount of adjustment stayed constant for two years across different sessions, likely reflecting

differences in calibration of solid standards among different labs, as well as values of accepted working reference gas standard. The analytical precision of the silicate standards was ±0.2 ‰ for $\delta^{18}O$ and ±0.01 ‰ for $\Delta'^{17}O$.

In a different set of runs, we loaded 2–4 mg of powdered samples into Ag cups and dried them overnight at 200 °C in a vacuum oven to drive away any absorbed water. δ^2H (δD) of bulk samples and amount of water was analysed by TCEA method, following the protocol in Hudak *et al*. (2022). We used a glassy carbon reactor and crucibles were held at 1450 °C in a He flow. Analyses were performed in a continuous flow mode and the data was reduced with respect to concurrently run water and slid standards (USGS mica and water welded in Ag tubes). Precision for δD is ±1–3 ‰ and 0.02–0.03 ‰ for $[H_2O]$tot.

Using bulk chemical composition of analysed rocks for correct $1000\ln\alpha^{18}O_{shale–water}$, $1000\ln\alpha^{17}O_{shale–water}$ fractionation equations

We used $1000\ln\alpha^{18}O_{shale–water}$, $1000\ln\alpha^{17}O_{shale–water}$, *vs*. *T* parametrisations as employed in Bindeman *et al*. (2018). Briefly, it finds the "bulk shale"- water curve based on estimated proportions of quartz (highest fractionation factor) *vs*. illite (lowest fractionation factor) by a linear combination of $A/T^2 + B/T$ equations, where coefficients are $A = 4.28 \times 10^6$ and $B = -3500$ for quartz (from Sharp *et al*., 2016) and $A = 3.8257 \times 10^6$ and $B = -5661$ for illite (reapproximated for low-T using two parameters after Zheng (1993) as in Bindeman *et al*. (2018). We used a parameter Q that ranges from 0 (100 % illite, most mafic shales) to 0.2 (20% quartz, 80% illite, most silicic shales in this database) to find $1000\ln\alpha^{18}O_{shale–water}$ fractionation equation for each sample. $1000\ln\alpha^{17}O_{shale–water}$ in this work was set to follow curvature for quartz as other minerals plot insignificantly above and below $\Delta^{17}O$ *vs*. $\delta^{18}O$ fractionation curves based on theoretical calculations (Schauble and Young, 2021).

In order to derive Q parameters, we used whole rock major element analysis of shales and CIPW norms. Then, we selected fractionation factors for all normative minerals from an online fractionation factor database (http://alphadelta.ggl.ulaval.ca) to compute weighted average mineral–water ^{18}O fractionation factors. Normative magnetite and corundum in CIPW norms were substituted with goethite and gibbsite as these minerals, as a best approximation, likely represented precursors in the protolith of shales and diamictites. Fractionation factors were later positioned on superimposed illite–water and quartz–water *vs*. temperature curves and were plotting in between these two endmembers with comparable curvature (*cf*. Bindeman *et al*., 2018). We used a meteoric water line equation from Luz and Barkan (2010) for the modern world, to numerically solve a system of two fractionation equations (for $^{18}O_{water}$, $^{17}O_{water}$) to compute $\delta^{18}O_w$ and $\Delta^{17}O_w$ and *T* in equilibrium with each sample. Note that an updated MWL from Surma *et al*. (2021) overlaps with Luz and Barkan (2010) equation in −3 to −30 ‰ $\delta^{18}O$ range. We used either bulk shale/diamictite values as input parameters, or "computed weathering product, WP" values, which were obtained by subtracting detrital igneous crust from each sample (+6.5 ‰, −0.06 ‰) by relying on CIA. Results of both calculations are shown in Table S-3, providing comparable values of computed equilibrium waters ($\delta^{18}O_w = -18.9$ ‰ and −20.9 ‰ respectively) and temperature (37.8 °C and 41.2 °C, respectively) of interaction for modern MWL by using bulk or weathering product input parameters. The meaning of the temperature is likely a combination of weathering and diagenetic signatures, and represent diffusional closure of water-rock interaction at ~2.9 Ga. We also present results of calculations for a different value of the mantle (SCO standard) of −0.052 ‰ (Sharp and Wostbrock, 2021) and such assumption result in −20 ‰ water at 32 °C. Sensitivity analysis was performed and results in ±3 °C and ±1.2 ‰ $\delta^{18}O_w$ difference between identical samples with Q ranging by 0.11.

We then used measured $\delta^{18}O$ and $\Delta^{17}O$ values, and an Archaean MWL equation $\delta^{17}O_w = 0.528 \times \delta^{18}O_w + 0.078$, corresponding to starting seawater value of −5 ‰ (as used in Bindeman, 2021). Results of these calculations give −26.3 ‰ $\delta^{18}O_w$ values and 7 °C temperature.

Effects of dehydration and then hydration on triple O isotopic value of rocks upon greenschist facies metamorphism: preservation of protolithic isotopic values

We consider measured whole-rock parameters $\delta^{18}O$, $\Delta^{17}O$ to be mostly reflecting the original breaking/creation of Si-O and Me-O bonds during weathering/diagenesis (e.g., Savin and Epstein, 1970; Bindeman, 2021) and that metamorphic

cycling would not change them significantly, while δD are affected more. We estimated potential effects of metamorphic devolatilisation on O and H isotopes by assuming a starting concentration of 6 wt. % H_2O in equilibrium with shale. Water content decreases to 2 wt. % while fractionation factors (tabulated in http://alphadelta.ggl.ulaval.ca) are following the T path, and fluid is removed in a Rayleigh manner. In all cases lighter $\delta^{18}O$ (heavier $\Delta^{17}O$) water is lost and heavier δD water is lost conforming to the sense of isotope fractionation (Sharp, 2017). Values of $\delta^{18}O$ increase by 0.4–0.52 ‰ and $\Delta^{17}O$ decrease by 0.004 ‰ in the residual rock regardless of batch *vs*. Rayleigh process (see Fig. 7 in Bindeman, 2021 for the magnitude of diagenetic changes in a Texas drillcore). Values of δD decrease by ~20 ‰ (Ripley *et al*., 1992). We did not consider the effects of dehydrogenisation (molecular H_2 loss, leading to heavier δD values; Kyser *et al*., 1986), nor effects of organic volatilisation.

If the subsequent dehydrated rock is hydrated upon retrogression, sources of fluids are likely mantle or crustal waters with $\delta^{18}O$, $\Delta^{17}O$ and δD values of ca. +6 ‰, −0.06 ‰ and +60 ± 20 ‰, respectively. Adding 2 wt. % of such water to an assemblage leads to an increase of 0.25 ‰ in $\delta^{18}O$, decrease of −0.002 ‰ in $\Delta^{17}O$ somewhat compensating devolatilisation changes, but causes an increase of up to 50 ‰ δD values, respectively. If a heavier (0 ‰) seawater were added it will lead to a heavier value.

Supplementary Tables

Table S-1 Hydrogen and oxygen isotope data.

Table S-2 Major element data (anhydrous basis) and CIA from samples of Klipwal Mine. Data of PNG2 sample from Ossa *et al*. (2018).

Table S-3 Computed temperatures and isotopic values of meteoric waters in equilibrium with samples computed with various assumptions shown.

Tables S-1 through S-3 (.xlsx) are available for download from the online version of this article at https://doi.org/10.7185/geochemlet.2319.

Supplementary Figures

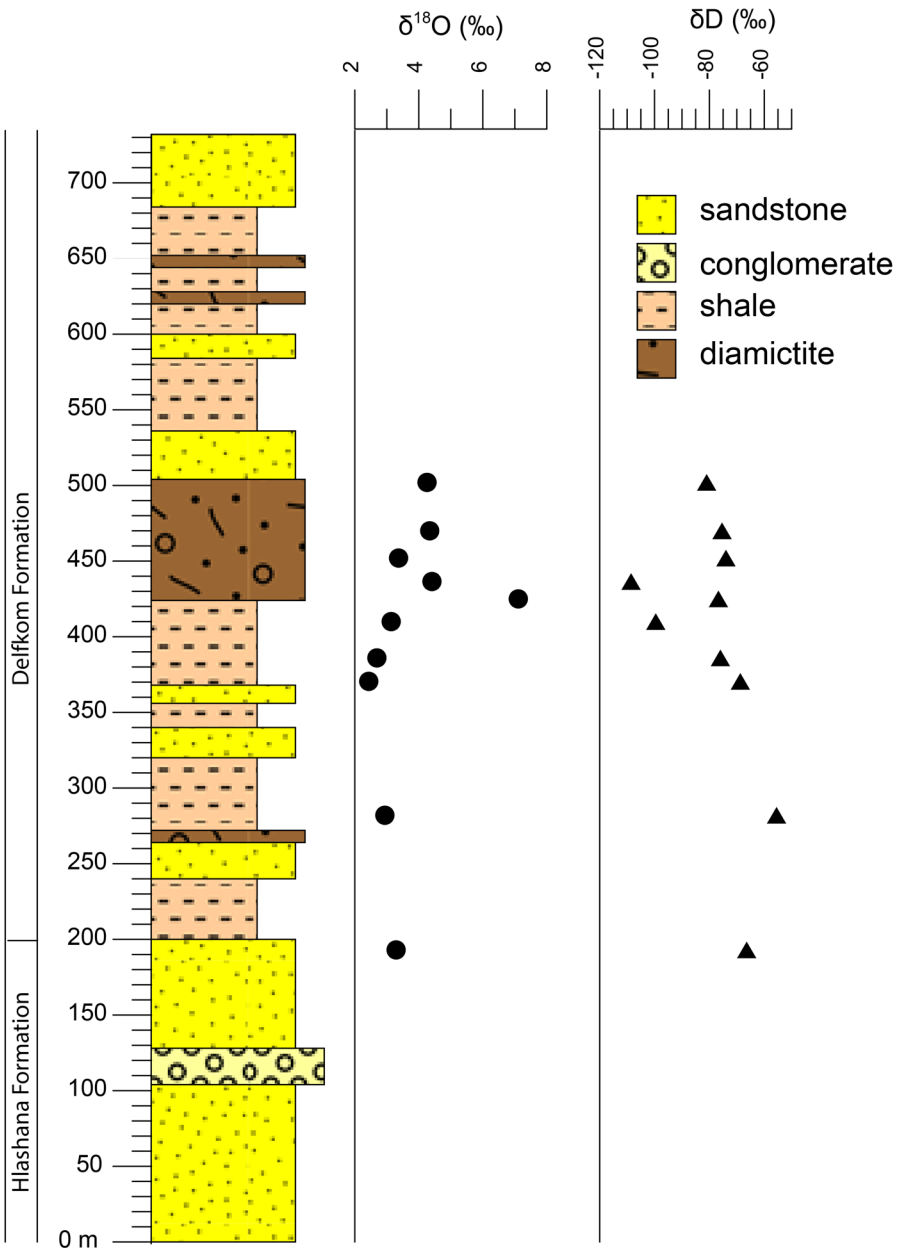

Figure S-1 Stratigraphic column of the top of the Hlashana Formation and overlying Delfkom Formation in the Klipwal Mine area (modified after von Brunn and Gold, 1993).

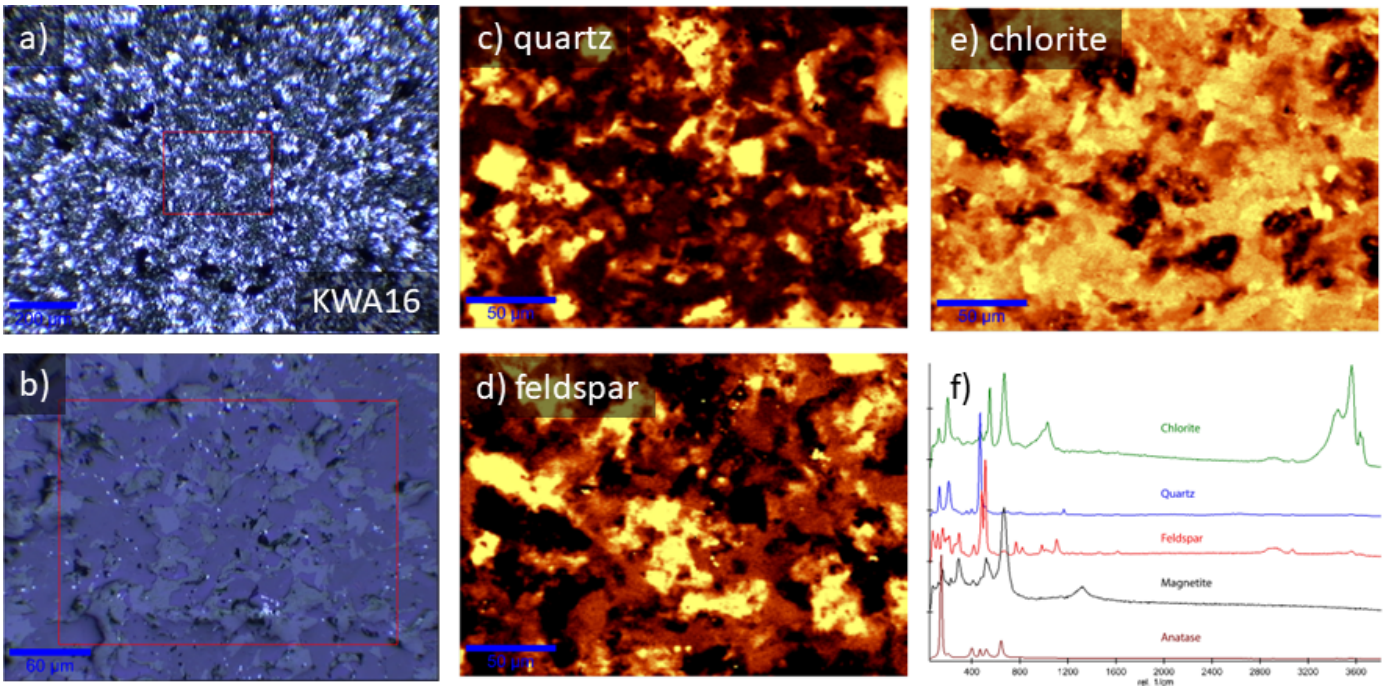

Figure S-2 Results of Raman spectroscopy of shale sample KWA16. **(a)** Photomicrograph in plane-polarised light; box shows the area shown in **(b)**. **(b)** Photomicrograph in reflected light; box shows the area of Raman mapping in subsequent images. **(c–e)** Raman maps showing the distribution of selected minerals. Brighter areas within Raman maps reflect higher intensities of mineral-specific spectra. Abundance of some minerals may be exaggerated due to peak overlaps. **(f)** Raman spectra of detected minerals.

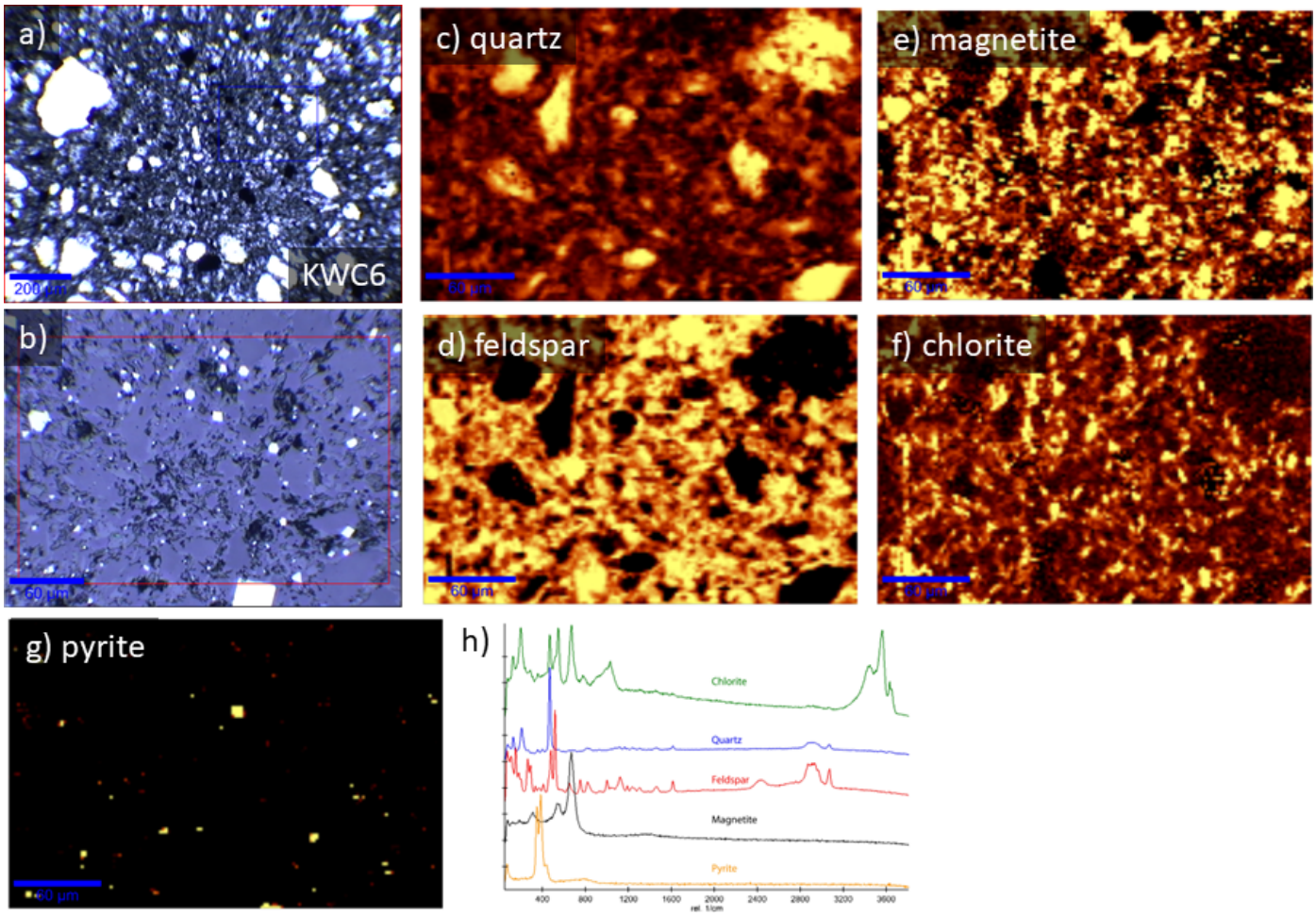

Figure S-3 Results of Raman spectroscopy of diamictite sample KWC6. **(a)** Photomicrograph in plane-polarised light; box shows the area shown in **(b)**. **(b)** Photomicrograph in reflected light; box shows the area of Raman mapping in subsequent images. **(c–g)** Raman maps showing the distribution of detected minerals. Brighter areas within Raman maps reflect higher intensities of mineral-specific spectra. Abundance of some minerals may be exaggerated due to peak overlaps. **(h)** Raman spectra of detected minerals.

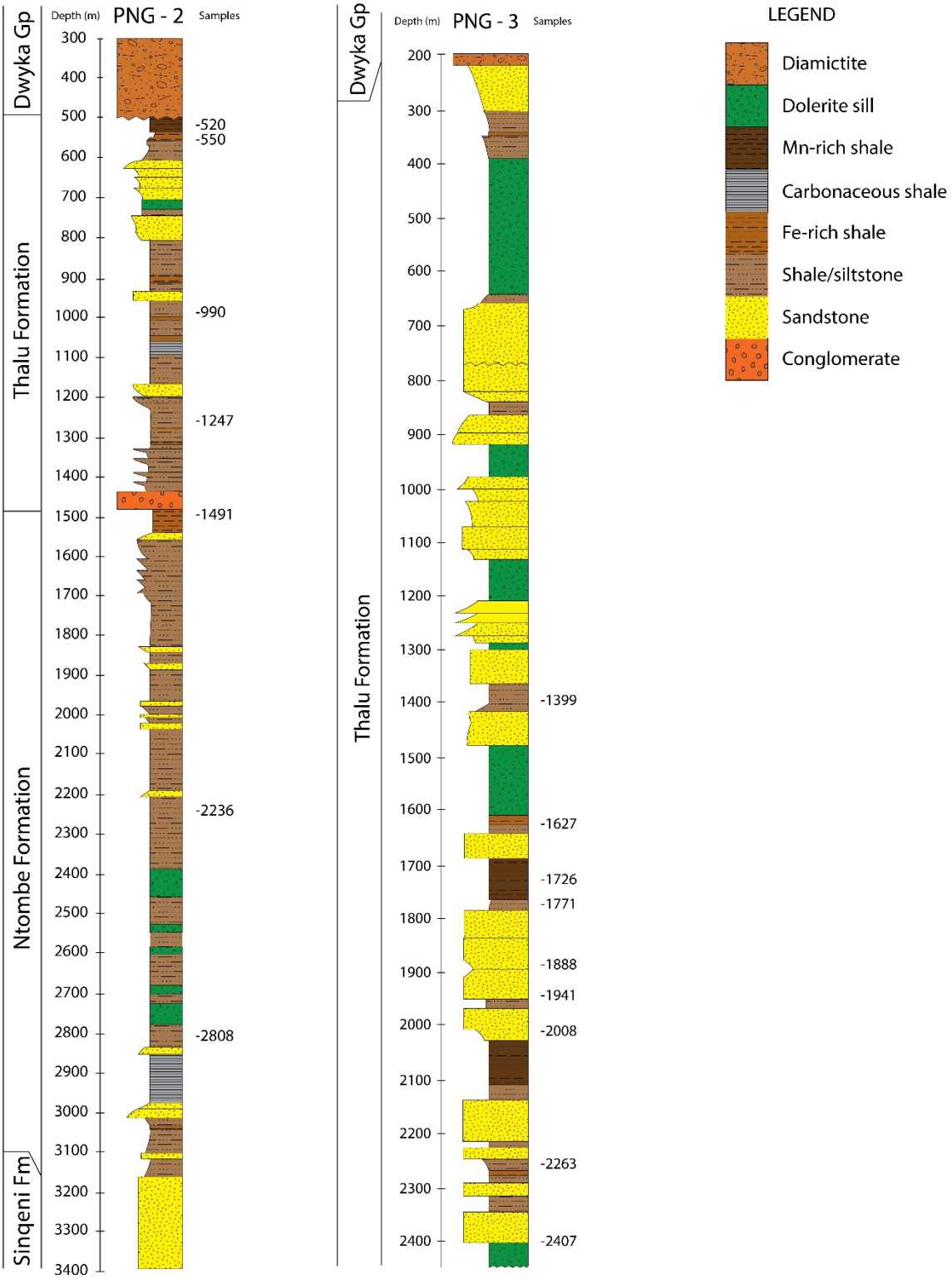

Figure S-4 Logs of borehole cores PNG 2 and PNG 3. Pongola strata are unconformably overlain by the Permo-Carboniferous Dwyka Group of the Karoo Supergroup.

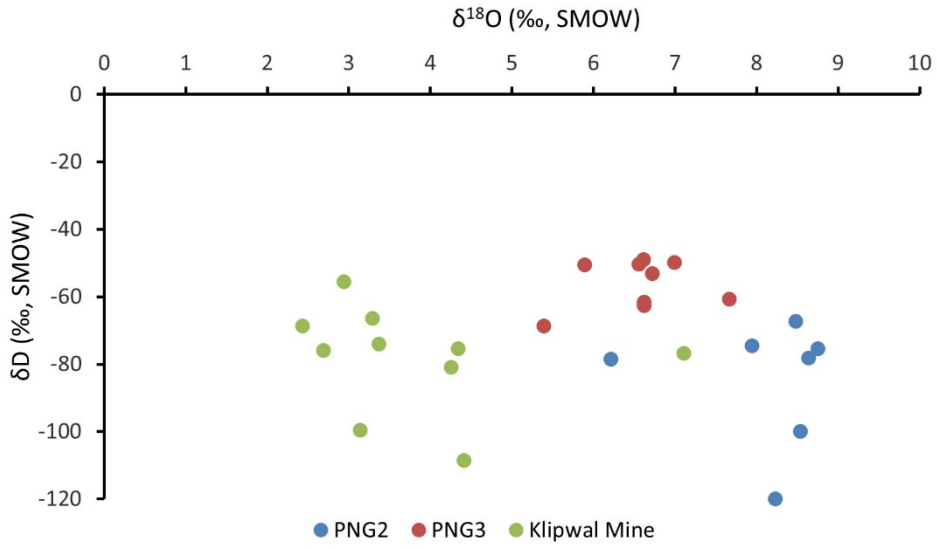

Figure S-5 Values of $\delta^{18}O$ *vs*. δD. Note the lack of correlation between the two isotope systems.

Supplementary Information References

Bindeman, I.N. (2021) Triple Oxygen Isotopes in Evolving Continental Crust, Granites, and Clastic Sediments. *Reviews in Mineralogy and Geochemistry* 86, 241–290. https://doi.org/10.2138/rmg.2021.86.08

Bindeman, I.N., Zakharov, D.O., Palandri, J., Greber, N.D., Dauphas, N., Retallack, G.J., Hofmann, A., Lackey, J.S., Bekker, A. (2018) Rapid emergence of subaerial landmasses and onset of a modern hydrologic cycle 2.5 billion years ago. *Nature* 557, 545–548. https://doi.org/10.1038/s41586-018-0131-1

Bindeman, I.N., Ionov, D.A., Tollan, P.M.E., Golovin, A.V. (2022) Oxygen isotope ($\delta^{18}O$, $\Delta'^{17}O$) insights into continental mantle evolution since the Archean. *Nature Communications* 13, 3779. https://doi.org/10.1038/s41467-022-31586-9

Hudak, M.R., Bindeman, I.N., Watkins, J.M., Lowenstern, J.B. (2022) Hydrogen isotope behavior during rhyolite glass hydration under hydrothermal conditions. *Geochimica et Cosmochimica Acta* 337, 33–48. https://doi.org/10.1016/j.gca.2022.09.032

Kyser, T.K. (1986) Chapter 5. Stable Isotopic Variations in the Mantle. *Reviews in Mineralogy and Geochemistry* 16, 141–164. https://doi.org/10.1515/9781501508936-010

Luz, B., Barkan, E. (2010) Variations of $^{17}O/^{16}O$ and $^{18}O/^{16}O$ in meteoric waters. *Geochimica et Cosmochimica Acta* 74, 6276–6286. https://doi.org/10.1016/j.gca.2010.08.016

Miller, M.F., Pack, A., Bindeman, I.N., Greenwood, R.C. (2020) Standardizing the reporting of $\Delta'^{17}O$ data from high precision oxygen triple-isotope ratio measurements of silicate rocks and minerals. *Chemical Geology* 532, 119332. https://doi.org/10.1016/j.chemgeo.2019.119332

Nesbitt, H.W., Young, G.M. (1982) Early Proterozoic climates and plate motions inferred from major element chemistry of lutites. *Nature* 299, 715–717. https://doi.org/10.1038/299715a0

Ossa, F.O., Hofmann, A., Wille, M., Spangenberg, J.E., Bekker, A., Poulton, S.W., Eickmann, B., Schoenberg, R. (2018) Aerobic iron and manganese cycling in a redox-stratified Mesoarchean epicontinental sea. *Earth and Planetary Science Letter*s 500, 28–40. https://doi.org/10.1016/j.epsl.2018.07.044

Ripley, E.M., Butler, B.K., Taib, N.I. (1992) Effects of devolatilization on the hydrogen isotopic composition of pelitic rocks in the contact aureole of the Duluth Complex, northeastern Minnesota, USA. *Chemical Geology* 102, 185–197. https://doi.org/10.1016/0009-2541(92)90155-X

Savin, S.M., Epstein, S. (1970) The oxygen and hydrogen isotope geochemistry of ocean sediments and shales. *Geochimica et Cosmochimica Acta* 34, 43–63. https://doi.org/10.1016/0016-7037(70)90150-X

Schauble, E.A., Young, E.D. (2021) Mass Dependence of Equilibrium Oxygen Isotope Fractionation in Carbonate, Nitrate, Oxide, Perchlorate, Phosphate, Silicate, and Sulfate Minerals. *Reviews in Mineralogy and Geochemistry* 86, 137–178. https://doi.org/10.2138/rmg.2021.86.04

Sharp, Z.D. (2017) *Principles of Stable Isotope Geochemistry*. Second Edition, Prentice Hall, Hoboken. https://doi.org/10.25844/h9q1-0p82

Sharp, Z.D., Wostbrock, J.A.G. (2021) Standardization for the Triple Oxygen Isotope System: Waters, Silicates, Carbonates, Air, and Sulfates. *Reviews in Mineralogy and Geochemistry* 86, 179–196. https://doi.org/10.2138/rmg.2021.86.05

Sharp, Z.D., Gibbons, J.A., Maltsev, O., Atudorei, V., Pack, A., Sengupta, S., Shock, E.L., Knauth, L.P. (2016) A calibration of the triple oxygen isotope fractionation in the SiO_2–H_2O system and applications to natural samples. *Geochimica et Cosmochimica Acta* 186, 105–119. https://doi.org/10.1016/j.gca.2016.04.047

Surma, J., Assonov, S., Staubwasser, M. (2021) Triple Oxygen Isotope Systematics in the Hydrologic Cycle. *Reviews in Mineralogy and Geochemistry* 86, 401–428. https://doi.org/10.2138/rmg.2021.86.12

Thompson, M., Potts, P.J., Webb, P.C., Kane, J.S. (1997) Geo*PT* - A Proficiency Test for Geoanalysis. *Analyst* 122, 1249–1254. https://doi.org/10.1039/A705095J

von Brunn, V., Gold, D.J.C. (1993) Diamictite in the Archean Pongola Sequence of southern Africa. *Journal of African Earth Sciences* 16, 367–374. https://doi.org/10.1016/0899-5362(93)90056-V

Zheng, Y.-F. (1993) Calculation of oxygen isotope fractionation in hydroxyl-bearing silicates. *Earth and Planetary Science Letters* 120, 247–263. https://doi.org/10.1016/0012-821X(93)90243-3